RESEARCH ARTICLE

A Comprehensive Study of Laboratory-Based Micro-CT for 3D Virtual Histology of Human FFPE Tissue Blocks

KIARASH TAJBAKHSH[1,2]**, ANTONIA NEELS**[1,2]**, ELENA FADEEVA**[3]**, JAKOB C. LARSSON**[4]**, OLGA STANOWSKA**[5]**, AUREL PERREN**[5]**, AND ROBERT ZBORAY**[1]

[1]Center for X-ray Analytics, Empa–Swiss Federal Laboratories for Materials Science and Technology, 8600 Dübendorf, Switzerland
[2]Department of Chemistry, University of Fribourg, 1700 Fribourg, Switzerland
[3]Waygate Technologies, 31515 Wunstorf, Germany
[4]Exciscope AB, 164 40 Kista, Sweden
[5]Intitute of Tissue Medicine and Pathology, University of Bern, 3008 Bern, Switzerland

Corresponding author: Robert Zboray (Robert.zboray@empa.ch)

ABSTRACT Advances in laboratory-based X-ray computed tomography (CT) have enabled X-ray 3D virtual histology. This method shows a great potential as a complementary technique to conventional 2D histology where extensive volumetric sampling is necessary. While formalin-fixed paraffin-embedded (FFPE) tissue blocks are the backbone of clinical histology, there exists no generic optimization, and technical study of the X-ray 3D virtual histology of FFPE blocks. X-ray micro-CT of FFPE blocks is studied and optimized in their native state within the cassette to minimize the interference of X-ray 3D virtual histology with clinical workflows and standards, hence facilitating the technology transfer to the clinics. The optimization is carried on the sample positioning, tungsten tubes acceleration voltage, and artifact reduction. Then propagation-based imaging of FFPE blocks is extensively discussed. Hierarchical (local) tomography and laminography are presented as viable approaches for achieving higher spatial resolutions. In the end, future perspectives are given by considering state-of-the-art micro-CT scanners using liquid-metal-jet sources, large-area detectors, and photon counting detectors. The results achieved here are generic and can be applicable to any laboratory-based scanner with a tungsten target source and cone-beam geometry. This article provides a starting point for anyone new to X-ray 3D virtual histology on FFPE blocks, but also serves as a useful source for more experienced users.

INDEX TERMS 3D virtual histology, computed tomography, formalin-fixed paraffin-embedded blocks, phase-contrast imaging, propagation-based imaging, transport of intensity equation, X-ray imaging.

I. INTRODUCTION

3D imaging of soft tissues is a topic of interest and the aim is to provide new insights into diseases phenotypes either for our fundamental understanding [1], [2], [3], or diagnostic

The associate editor coordinating the review of this manuscript and approving it for publication was Chih-Yu Hsu.

purposes [4]. Various methods are used, such as destructive 3D reconstruction of serial wholes slide images [5], or chemically intrusive techniques like light sheet, confocal, or two photon microscopy [6]. Recently, X-ray micro-CT is receiving attention for histological applications [7]. It is non-destructive, and requires minimal sample preparation. While clinical CT has traditionally been used to scan dense

specimens with macroscopic features of interest (>0.5mm), recent advances in X-ray technology have allowed for sub-micron spatial resolution and improved soft-tissue contrast [7], [8], [9], [10], [11]. All these methods provide 3D images of the specimen with their own characteristics, and none is overall superior to the others.

Attenuation based X-ray imaging has a limited ability to distinguish between materials with a little difference in electron densities or low X-ray attenuation such as soft tissues. X-ray phase-contrast imaging (XPCI), on the other hand, uses phase-shift of the X-ray wavefront imposed by the specimen, resulting in up to 1000 times improvement in contrast-to-noise ratio (CNR). This allows feature visibility in the images of internal structures that are otherwise difficult to distinguish. Propagation-based imaging (PBI) is the most commonly used XPCI technique. Initially PBI was believed to be limited to synchrotron facilities [12]. Although synchrotron-based PBI can greatly increase our fundamental understanding of biological systems [13], [14], due to its limited accessibility it cannot be used as daily diagnosis tool in the clinics. Fortunately, PBI was made possible in laboratories because of advances in microfocus X-ray sources [15]. A comparison between latest generation of X-ray scanners devices, and 3rd generation beamlines shows that laboratory settings are coming closer to the image quality provided by synchrotron imaging beamlines [16]. Of course the scanning times on the laboratory-based devices are significantly longer. Nonetheless, due to accessibility and commercial availability of laboratory-based scanners, soft-tissue X-ray imaging for every-day clinical use is now a possibility [17], [18], [19], [20].

In this context, the importance of formalin-fixed paraffin-embedded (FFPE) blocks 3D imaging techniques has been pointed out previously [6]. FFPE blocks allow for large scale studies on preserved tissues spanning back over a century, providing novel insights on improved diagnostics and diseases understanding and could be especially beneficial in the context of precision oncology. Clinical applications of X-ray 3D virtual histology and its correlation with conventional histology has been already demonstrated [21], [22]. It is advantageous in a broad range of applications from larger volumes with morphological features of interest, such as follicular thyroid carcinoma [21], [4], as well as cellular resolution, e. g. brain tissue [23]. Diagnostic values of micro-CT for tissues with good absorption contrast are well known, e. g. lung [24], [25], and micro calcification in breast tissue [26]. XPCI is expanding the area of applicability of X-ray virtual histology beyond the tissues with good attenuation contrast [27]. For examples, XPCI has been used for 3D imaging of mouse heart [28], articular cartilage [29], blood clots [30], and neurodegenerative diseases [31].

FFPE blocks represent an important pillar and object for the further development of 3D X-ray virtual histology and potential clinical transfer. As the embedding protocol and storage standards are not likely to change in the clinical practice, in order to facilitate a seamless integration of X-ray 3D virtual histology at the clinics X-ray virtual histology studies should be carried on FFPE blocks within the embedding cassette. The presence of cassette and wax around the tissue is unavoidable on standard FFPE block used in the pathology and they can contribute to artifacts and suboptimal conditions for the imaging. First, the slit-like cassette grid structure, gives rise to pronounced cone-beam artifacts [32], [33], and second, the wax around the tissue reduces contrast of the soft tissue compared to air-tissue interface and the non-negligible amount of wax around the tissue in an FFPE blocks results in parasitic X-ray absorption decreasing image quality, signal-to-noise-ratio and CNR [34]. Also, removing the tissue and re-embedding is a destructive and cumbersome step that optimally should be avoided.

There exists a basic user guide for soft-tissue X-ray imaging [35], as well as a coarse preliminary study on standard operating procedure for using micro-CT in a broader context in pathology [36]. A comprehensive optimization study and an overview of the technical possibilities that could serve as a technical guide, with an eye on more advanced methods and future developments while considering the above aspects is still missing. For full exploitation of X-ray based virtual histology, here we address the technical possibilities and issues, relevant artifacts as well as, their mitigation. Initially, micro-CT for FFPE blocks is optimized with respect to X-ray tube acceleration voltage and CNR for a variety of tissues. Namely, follicular thyroid carcinoma, Bladder, Pancreas, and lung cancerous tissues FFPE blocks where a global optimum value for tungsten target tubes voltage is established. Then optimal geometry for propagation-based imaging (PBI), and its range of validity based on estimated visibility by the transport-of-intensity equation (TIE) is given. Afterwards, Paganin phase-retrieval and Bronnikov-aided correction (BAC) algorithms are discussed and demonstrated for FFPE blocks. Then, possibilities for high-resolution imaging such as hierarchical (local) tomography, and laminography of FFPE blocks are presented. Finally, future perspectives and outlooks for further developments of 3D X-ray based virtual histopathology on FFPE blocks regarding recent advances in laboratory X-ray scanner hardware are given.

We note explicitly that our goal here is to focus on the technical details and optimization of the method. Therefore refer the reader for a detailed elaboration on the clinical aspects and benefits of our approach, also in the context of precision medicine, for the case of follicular thyroid carcinomas to our previous publication [4].

II. MATERIALS AND METHODS
A. FFPE BLOCKS
Throughout the manuscript follicular thyroid carcinoma FFPE blocks are used as a representative example unless stated otherwise. Tissue Biobank Bern (TBB) manages tissue samples and patient information according to respective regulations and fulfills the Swiss Biobanking Platform requirements. The Institute of Tissue Medicine and Pathology

(ITMP) of the University of Bern provided the samples and pseudonymized patient data from the TBB according to the protocol approved by the cantonal ethics commission (KEKBE 2018-01657).

B. X-RAY MICRO-CT

The main body of the study was carried out using a commercial micro/nano-CT device, EasyTom XL Ultra (RxSolutions SAS, Chavanod, France). The scanner features a Hamamatsu reflection target microfocus X-ray source L10801 hereinafter referred to as reflection target tube. The bremsstrahlung emission spectrum of this tube as a function of the tube acceleration voltage was simulated using [37], and the result is provided in the supplementary materials Fig. S1. The scanner also features a Hamamatsu transmission nano focus X-ray tube L10712-02 that is suitable for submicron resolution scans and is not used within this study.

The detectors available are a flat panel (FP) detector with a thick, high-efficiency CsI scintillator, $127\mu m$ pixel size with an 1880×1494 pixels configuration and 16-bit dynamic range. The other detector is a 14-bit charged coupled device (CCD) fiber optically coupled to a $20\mu m$ Gadox scintillator. The native pixel size is $9\mu m$ with 4008×2672 pixels, but it is used in 2×2 binning ($18\mu m$) as the best physical resolution attainable is limited by $20\mu m$ thick Gadox scintillator. Furthermore, the spatial resolution of the detector throughout the manuscript is defined by the width of its point spread function (PSF) being ca. 2.4 times the physical pixel size, which is determined experimentally both for the FP and the CCD. Normalized spectral sensitivity of the detectors were simulated using XCOM NIST dataset [38], and are available in the supplementary materials Fig. S1. For simplicity, from now on these detectors are referred to as FP and CCD, respectively.

A commercial Feldkamp-Kress-Davis implementation for cone-beam CT [39], in the software Xact by Rx-Solutions (Chavanod, France) was used for reconstruction. This results in isotropic voxels and we use hereafter voxel size for designating the edge length of such isotropic voxel.

III. WHOLE BLOCK SCAN

A. POSITIONING

Proper sample positioning during tomography is critical to maximize image quality. There are two potential mounting modes for the FFPE block, namely "vertical" and "horizontal" presented in Fig. 1. In the vertical configuration, the surface normal vector of the wax is perpendicular to the rotation axis y, and in the horizontal configuration, surface normal vector is parallel to the rotation axis y. In this section, we cover the advantages and disadvantages of both FFPE block positioning.

B. TUBE VOLTAGE AND CNR

The tube voltage determines the emitted photon energies and thus the probability of their interaction with the specimen.
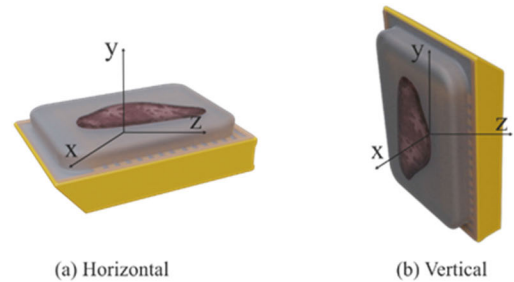
FIGURE 1. Two FFPE tissue block orientations possible for scanning. Rotations and optical axis are y, and z, respectively. In yellow the cassette of the block, and in gray the wax are shown.

Therefore, it is an essential parameter to optimize for obtaining, high-contrast, low noise images.

On one hand, one can expect higher contrast at lower photon energies due to the larger differences in the attenuation coefficients. On the other hand, one can expect less noise as a result of higher photon flux at higher X-ray tube voltages. Therefore, we use CNR as a comprehensive figure of merit to consider. CNR at variable tube voltages is investigated for two mounting modes presented in Fig. 1. Standard definition is used, $CNR = |\bar{I}_2 - \bar{I}_1| / \sqrt{\sigma_2^2 + \sigma_1^2}$, where subscripts refer to the selected regions of interests (ROIs) in a homogenous region of soft-tissue, and the ambient paraffin wax with equal areas. $\bar{I}$, and σ denote the ROIs' mean gray value and standard deviation, respectively.

Here the optimal positioning for maximizing CNR with respect to tube voltage is investigated. We maintained consistent scan geometry, imaging resolution, and detector parameters throughout the investigation. The tube power is kept constant at 20W by changing tube current according to the varying tube voltage. The tube voltage ranged from 40kVp to 90kVp in 10kV increments, and the CNR was assessed at each step. According to the manufacturer, these settings provide a constant tube spot size of $15\mu m$ across the measurements. Detailed scan parameters are available in Table S1 and Table S2 in the supplementary materials.

According to the Kramer's rule the effective photon energy for a Bremsstrahlung spectrum is at ca. 1/3 of the kVp and the majority of the photons are around and below this energy. Within the above photon energy range we get a sufficient penetration of the FFPE blocks in both positioning, to enable good photon statistics on the detector. As for the upper tube voltage limit, it is well-known that for increasing photon energy the attenuation contrast, especially for soft tissues, drastically diminish as the dominant photon-matter interaction process is the photoelectric effect, whose probability goes inversely by the cube of photon energy (E^{-3}). On the other hand, bremsstrahlung radiation brilliance drops considerably below 40kV tube voltage resulting in poor photon economy. Besides, experience shows and vendor information confirms that the X-ray tubes spot becomes less focused and unstable at low ($<$40kV) tube voltages.

Therefore, no optimal tube voltage beyond the above values is anticipated.

According to Fig. 1 horizontal, and vertical position contrast are maximal at 40kVp (11277±20, and 13023±17, respectively) and decreases with increasing voltage as expected. Fig. 1(a) shows CNR peaks between 50kVp to 60kVp for the horizontal position due to the trade-off between attenuation-contrast and photon flux. Overall, vertical positioning results in higher CNRs. As illustrated in Fig. 2(b), the highest CNR is achieved at 40kV for vertical sample setting. On the other hand, the horizontal position generally yields lower CNR values due to lower mean photon flux for most of the projections as the X-ray beam have to penetrate more wax and tissue.
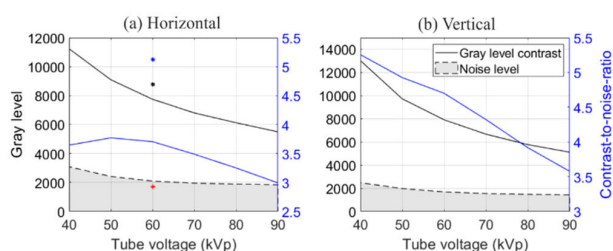
FIGURE 2. CNR versus tube voltage in (a) horizontal and (b) vertical mounting modes. Left y-axis is gray level and shows the contrast (solid line), and noise level (gray area with dashed border). Blue y-axis in the right is the CNR. Black, red, and blue stars in (a) are contrast, noise, and CNR for 60kVp double-time scan, respectively. The error is calculated as the mean of standard deviation and in the both plots, the error of the contrast, noise, and CNR remain below 0.2%, 0.7%, and 1.0%, respectively.

Note pairing two blocks, i. e. with their respective wax surfaces facing each other enables higher throughput scanning, which can be a significant benefit for scanning larger sample cohorts. Or alternatively higher quality scans as one can double the scanning time when pairing two FFPE blocks without increasing the overall cohort scan time. This results in the CNR improvement of ca. 1.42 times, as demonstrated by star points in Fig. 2(a). Considering the above improvement in CNR and the data in Fig 2, we can conclude that scanning in the 50kVp to 60kVp range, paired in horizontal positioning is the optimal setting for scanning a large FFPE sample cohort, whereas individual vertical positioning of the blocks result in a slightly better CNR. Therefore, placing the FFPE block vertically should be preferred when an individual block is being scanned. Paring in vertical position significantly increases the parasitic photon attenuation in the two relatively attenuating cassettes diminishing the CNR (whereas in horizontal paired configuration one has to penetrate the same amount of wax and tissue as for single blocks), thus representing a clearly suboptimal option. Furthermore, it would also accentuate certain artifacts only attributed to vertical positioning, like e.g. the Defrise artefacts discussed below.

As FFPE blocks are well standardized in size shape and embedding materials, we expect our results to hold and be applicable for a broad range of different tissues. To investigate

this, we ran the same analysis for lung, bladder, and pancreas cancerous tissue FFPE blocks in horizontal mounting mode, and the same CNR peak in the range of 50 to 60kVp was observed. These results and some illustrative images showing ROIs used for the CNR calculation are provided in the supplementary materials Fig. S2 and Fig. S3.

C. DEFRISE ARTIFACT
Defrise artifact is inherent to the cone-beam tomography, resulting from a missing cone of information in the frequency domain [33]. In case of FFPE blocks, the slits in cassette grid structure give rise to pronounced Defrise artifact manifesting itself in horizontal stripes. This artifact is specific to vertical sample positioning, presented in Fig. 3(a), whereas, it does not appear for horizontal sample positioning.
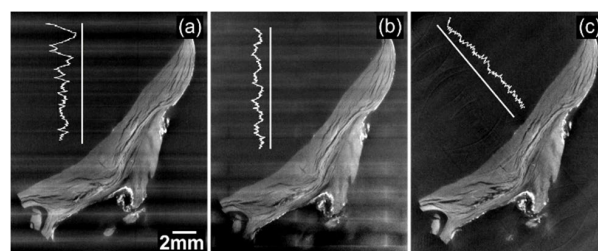
FIGURE 3. (a) Circular trajectory cone-beam CT where Defrise artifacts are most pronounced. (b) Pseudohelical CT reconstruction produces a uniform Defrise artifact across the vertical span. (c) Tilted FFPE block, rotating the FFPE block around its wax surface normal vector in circular trajectory CT efficiently damps Defrise artifact. In white the profile along the straight white lines is shown to illustrate the strength and profile of Defrise artefacts.

There exist both numerical and experimental methods in the literature for reducing cone-beam artefacts. Numerically, iterative reconstruction methods have been reported to reduce Defrise artifact [29]. We opted for experimental approaches for Defrise artifact correction. First approach is helical tomography. It is known if the pitch is selected carefully, it is supposed to provide a fully sampled Fourier space that eliminates the Defrise artifact [30]. In Fig. 3(b) a two turn (2×1440 projections) pseudohelical tomography is presented with similar scanning parameters as Fig. 3(a). EasyTom XL ultra scanner doesn't feature a helical tomography reconstruction using the Katsevitch method [30], rather it uses a proprietary modified FDK algorithm. In our pseudohelical tomography, Defrise artifacts still exist but they are evenly distributed compared to the cone-beam case.

The second approach, well-known from literature for Defrise phantoms is to tilt the FFPE block around the surface normal vector of the FFPE block [31]. In Fig. 3(c) the block was rotated at an angle of 39 degrees, which causes the spatial frequency representation of the cassette grid structure to lie outside of the missing information cone of cone-beam tomography. Although there are still some Defrise artifacts present, the amplitude is negligible. Tilting is an optimal approach for minimizing the Defrise artifact while maintaining faster acquisition of the circular trajectory compared to helical trajectory tomography.
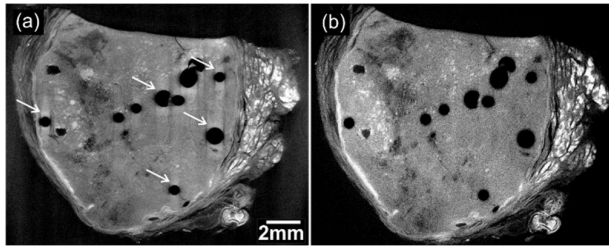
FIGURE 4. Vertical sample positioning is prone to streak artifact. (a) Vertical positioning. White arrows show streak artifact around regions with abruptly changing material properties. (b) Horizontal positioning shows no streak artifacts. Note that the circular, dark, air-filled areas are either air bubbles due to imperfect casting process of the FFPE block or core-out areas used for creating tissue micro arrays.

D. STREAK ARTIFACT

The vertical positioning can produce streaks around edges of regions with abruptly changing materials properties like at air bubbles/cored-out sections interfaces with the wax. White arrows in Fig. 4(a) indicate streak artifacts. The streaks essentially originate from the Gibbs phenomenon triggered by a sudden change in the material properties. These sudden changes are pronounced in most of the projection images for a vertical sample positioning. In contrast, this effect is suppressed for horizontal sample position by more uniform and higher thickness of the sample across projections, effectively damping the sudden step changes in the specimen attenuation, as shown in Fig. 4(b).

E. SCATTERING ARTEFACT

Horizontal pairing of two FFPE blocks results in strong bright-dark streak (fringe) for each block close to their top surfaces (the ones facing each other) as is shown in Fig. 5(a) by white arrows on the YZ, and XY isoslices and illustrated by the white dashed area on the XZ slice. This is a combination of the edge-enhancement (refraction) and small angle scatter effects originating from the slightly oblique top surface of the opposite block. Practically, this can be eliminated by placing an X-ray transparent spacer, e.g. Styrofoam, between the blocks. This introduces a spacing between the blocks so these artefacts are not appearing in the CT slices of the individual blocks. Note that white spots/lines in between the samples indicated by white arrows on Fig. 5(b) are small contribution from the not fully transparent.

Styrofoam and they do not influence the individual images of the blocks. The slight quality difference between Fig. 5(a), and (b) is due to difference in scan times. Detailed scan parameters are available in Table S3.

In summary, optimal settings for the scanning FFPE block for 3D virtual histology depends on the individual application, sample cohort size and time available. While, vertical positioning produces better CNR, horizontal positioning produces less artifacts and allows for paring two blocks for faster and more efficient scanning. Therefore, for high-throughput applications horizontal pairing should be preferred. In such cases, the application of a thin Styrofoam

spacer helps to eliminate scattering artifacts. If one selects vertical mode, Defrise artifact can be effectively eliminated by rotating the block around its surface normal vector. Meanwhile streak artifact around air bubbles will still be present.

IV. PROPAGATION-BASED IMAGING ON FFPE BLOCKS

In XPCI, one exploits the phase-shift in the X-ray wavefront ($\varphi = 2\pi/\lambda\delta t$) upon propagating through a material of thickness t with a refractive index $n(\lambda) = 1-\delta(\lambda)+i\beta(\lambda)$, where λ is the wavelength. The ratio of the decrement of the real to the imaginary part of the refractive index (δ/β) is typically up to 1000 at hard X-ray wavelengths, making the phase-shift a significantly more sensitive contrast modality than the attenuation-contrast. However, measuring wavefront phase-shift is not straight forward, particularly at hard X-ray energies since optical elements are much more difficult to realize than for the visible regime. As well as limited brilliance and coherence of laboratory-based X-ray sources.

There exist several XPCI methods, namely, Talbot interferometry or so called grating-based [40], [41], edge-illumination [42], and speckle-based imaging [43]. Propagation-based imaging (PBI) is the most commonly used XPCI technique due to its simplicity, and compatibility with a range of facilities [44]. PBI highlights refractive index gradients (edges) through Fresnel-diffraction effects and this phenomenon is commonly referred to as edge-enhancement. A prerequisite of all XPCI techniques is some degree of radiation coherence and PBI is no exception. Temporal coherence (monochromacity) requirements of PBI are relaxed, facilitating use of broad-spectrum laboratory sources, but a source with a certain degree of spatial coherence is required which can be typically met with micro/nano focus X-ray tubes [44].

A. GEOMETRICAL OPTIMIZATION OF PBI FOR FFPE BLOCKS

PBI can be mathematically described by transport of intensity equation (TIE), indicating that by propagating the wavefront, the intensity distribution is modulated by gradient and Laplacian of the wavefront phase delays [45]. TIE also implies that, this intensity modulation scales linearly with effective propagation distance. For cone-beam geometry imaging, Fresnel scaling theorem implies that the effective propagation distance is nonlinear with respect to source detector distance (SDD), and source object distance (SOD), and is defined as $Z_{eff} = (SDD-SOD)/M$, where $M = SDD/SOD$ is the geometrical magnification. As a result, the edge-enhancement is maximal at SOD = SDD/2 for cone-beam micro-CT. This theoretical optimum for an ideal imaging system is not always applicable in practical situations. It has been shown if one takes into account imperfections of the imaging system [46], [47], there exist an optimal SOD for maximal edge-enhancement as a function of SDD, and imaging system point spread functions (PSF). This can be approximated for a near perfect
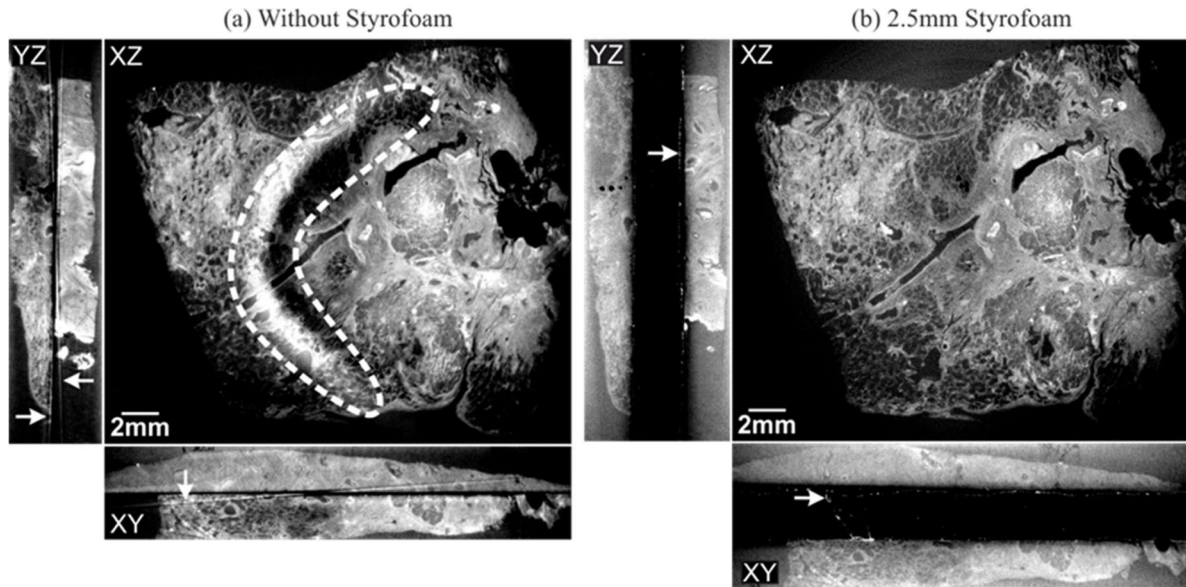
FIGURE 5. Scattering artifact corrupts the first few top slices of each block in horizontal positioning of blocks scanned in pairing mode. (a) Shows isoslices when the two blocks placed directly on top of each other. White arrows indicate the fringe in YZ and XY slices, and white dashed area shows the fringe in XZ slice. (b) The same specimen scanned with a 2.5mm thick Styrofoam spacer between the FFPE blocks. The scattering artifact is eliminated but there are small contributions from Styrofoam pointed out by white arrows. However, these contributions do not affect the CT images of the individual blocks. The specimen presented here is lung cancer tissue.

edge $\sigma_{\text{edge}} \ll (\sigma_s^2 + \sigma_d^2)^{1/2}$) as

$$\text{SOD}_{\text{opt.}} \cong SDD \left(\frac{\sigma_s^2}{\sigma_s^2 + \sigma_d^2} \right)^{1/2} \qquad (1)$$

where σ_d, σ_s are standard deviation of the Gaussian functions describing detector and source PSFs, respectively. Eq. (1) implies that for $\sigma_d = \sqrt{3}\sigma_s$, $\text{SOD}_{\text{opt.}}$ reduces to SDD/2 which is the maximal Z_{eff}. Therefore, most optimal imaging device for PBI must satisfy this condition. This more realistically achievable for laboratory micro-CT scanners applying two-stage magnification (the second one is optical and realized on the detector) but less for larger- pixel FP detectors with no optical magnification. The latter, however, typically having significantly higher detection efficiency.

To evaluate the dependence of the edge-enhancement on geometrical parameters for our experimental setups in our EasyTom XL Ultra we follow the methodology in [46]. The TIE for a near perfect edge was simulated and the MATLAB script can be found in [48]. We assumed a near perfect edge, and monochromatic radiation at 15 keV as is the mean energy of our X-ray tube at 40kV. Tube focal spot is assumed to be 5μm as provided by manufacturer. As a simplification, a 2.5mm thick pure phase specimen (i.e. n =1-δ with δ =1 $\times$ 10.6) was considered. Furthermore, we assume σ_d = 2.4$\times$ pixel size as it was experimentally measured for our detectors. Our running parameters are SDD and SOD to investigate the optimal geometries for PBI, and its region of validity for FFPE blocks for our two different detectors: the CCD with its small and the FP with its large physical pixel size.
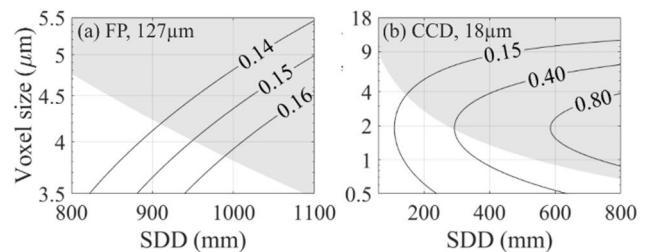

FIGURE 6. Contour plots of the edge-enhancement visibility vs geometrical settings of the scanner. We assume visibility level above 0.15 is detectable. (a) FP with 127 μm, and (b) CCD with 18μm physical pixel size. Gray area indicates achievable geometrical parameters on our scanner limited by the 30mm minimum SOD imposed by the FFPE block dimensions.

Fig. 6(a) shows the edge-enhancement visibility map for the FP, and that of CCD is shown in Fig. 6(b). It is clear from the maps that the CCD enables higher visibility of edge-enhancement for similar SDD and image voxel sizes due it its smaller physical pixel size. The smaller pixel size allows for larger Z_{eff}, hence the edge-enhancement visibility is greater. For the CCD edge-enhancement visibility peaks at about 2.00μm voxel size, not far from 2.06μm following from the $\text{SOD}_{\text{opt.}}$ given by Eq. (1). The gray area highlights achievable voxel sizes with respect to minimum SOD possible (ca. 30mm) imposed by the sheer size of an FFPE block at a given SDD.

For the FP, the visibility of the edge-enhancement is generally lower than our imposed limit. However, at sufficiently long SDD, i. e. SDD $>=$ 1000mm, and optimal magnification the edge-enhancement is visible at the 0.15 threshold as is shown by the contour plot in Fig. 6(a) and supported

experimentally by Fig. 7(e). This also indicates that PBI is pronounced enough only at sufficiently small voxel size for a 127μm FP detector. To get such voxel size is not possible for the whole FFPE block due to the limited field of view (FoV) of our FP. However, edge-enhancement on whole block level is possible with a larger detectors with large pixel sizes (ca. 100μm) as will be demonstrated in the future perspective section.
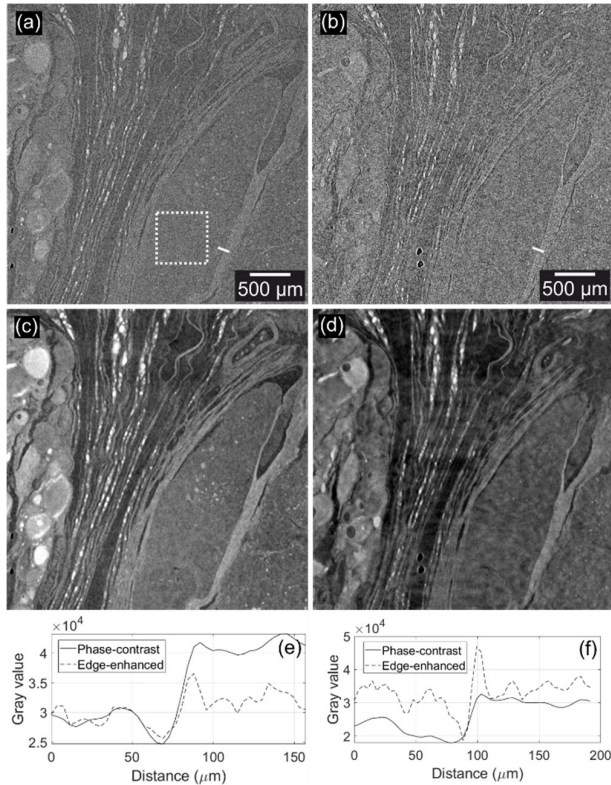
FIGURE 7. PC imaging on a FFPE block (a) edge-enhanced attenuation image by FP, and (c) its corresponding PC image obtained by the Paganin phase retrieval. (b) CCD edge-enhanced image, and (d) its corresponding PC. (e) and (f) are the edge profile comparison between edge-enhanced images in (a), and (b), and their counterparts in the phase retrieved images, (c), and (d). The respective edge is indicated by a white line of 25 pixels thickness in (a) and (b). Selected edge is a transition from cancerous tissue to tumor capsule of follicular thyroid carcinoma.

In conclusion, it is not possible to perform PBI on the whole block level using a small detector with large pixel size similar to the presented FP. However, a possible strategy would be to first perform a scan at the whole block scale (ROI $\simeq 30 \times 20$mm^2) choosing a minimal SDD that prioritizes photon statistics and absorption contrast. Then a local scan can be performed on the ROI at smaller voxel sizes that allow utilization of edge-enhancement and phase-contrast as well as resolving the feature of interest with greater details. On the other hand, the most optimal approach where the tissue under examination does not poses a sufficient absorption contrast, could be to employ a small pixel size detector such as the CCD presented in the current study. As demonstrated in Fig. 6(b) such a detector is much more suitable for having a well pronounced edge-enhancement. This could unravel

structures that are otherwise difficult to appreciate using only attenuation contrast.

B. PHASE-RETRIEVAL ALGORITHMS

The edge-enhanced image strongly highlights interfaces, and abrupt changes in the specimen but its is not a phase-contrast (PC) image. One can construct the PC image based on edge-enhanced image using phase-rertieval methods. The only practical method in laboratory setup is the single-distance phase retrieval, which leads to the inverse problem of phase-retrieval with insufficient information [49], [50]. This is resolved by applying simplifying assumptions of which the most widely used method is the Paganin phase-retrieval, assuming single material object ($\delta/\beta =$ Constant), but allowing for varying material density [50]. Only under these conditions quantitative phase retrieval is possible, otherwise PC images provide contrast-enhanced qualitative images, which prove to be also very useful in many practical applications. Although the underlying assumption is rarely met in reality, Paganin retrieval is widely and successfully used for a broad range of samples [51], [52], [53].

We use an implementation of the Paganin phase-retrieval in the XAct software by Rx-Solutions (Chavond, France), where the phase-retrieval parameters are lumped and expressed in terms of Paganin filter cut-off frequency at -6dB. As a common practice for broad-spectrum laboratory sources, the cut-off frequency is tuned manually by visual inspection of the image [19]. Fig. 7 shows two edge-enhanced images acquired with the reflection tube. Fig. 7(a) is captured with the FP, and Fig. 7(c) is its corresponding PC image. Fig. 7(b) is captured with CCD, and its PC image is shown in Fig 6(d). Fig. 7(e) and (f) show the line profile along the white line in Fig. 7(b) being averaged over its 25 neighbouring pixels. CNR of the images in Fig. 7 were calculated between a region of soft tissue, shown by dashed rectangle in Fig. 7(a), and a same sized area of the paraffin wax selected deeper in the FFPE blocks. CNR values prior and after to phase-retrieval are presented in Table 1. There is a 14 fold improvement in CNR in Fig. 7(d) while it's a 6 fold improvement for that of Fig. 7(c). Showing the significance of smaller pixel sizes for FFPE block PBI. Detailed scan parameters are available in Table S4.

The modified Bronikov algorithm, (MBA) is another phase retrieval algorithm that assumes low absorption as the basis for its derivation [54]. Ultimately, MBA and Paganin formulations have a similar mathematical structure. Therefore, we deemed it unnecessary to present results using the MBA here. However, there exists Bronikov aided correction (BAC) that treats edge-enhancement as an artifact and eliminates it by utilizing retrieved PC image by MBA. It does so by reconstructing a contact image ($Z_{eff} = 0$) [55]. Although BAC is not producing a PC image, it has been observed that BAC enhances CNR, and performs surprisingly well on biological specimen [56]. For BAC method one has to optimize two parameters one is related to MBA step (α)
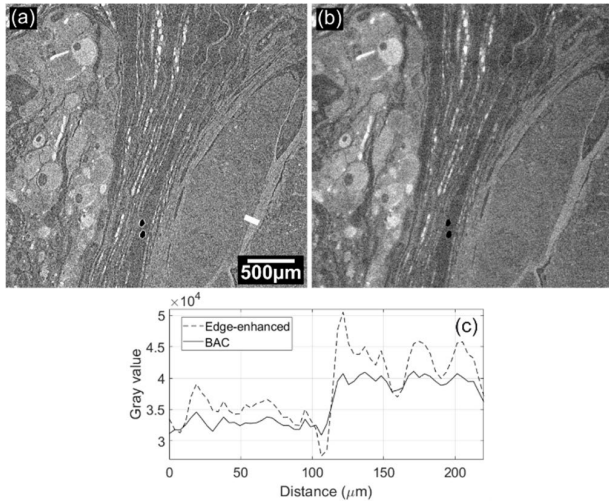
FIGURE 8. Comparison of (a) edge-enhanced image, and (b) BAC with $\alpha =$ 0.07, and $\gamma = 4$. The scan is the same as the one presented in Fig. 6(a). (c) shows line profiles along the white line presented in (a).

TABLE 1. CNR values of Fig. 6 and 7.

Detector	Paganin cut-off frequency	$CNR_{Att.}$	CNR_{PC}	$\frac{CNR_{PC}}{CNR_{Att.}}$	CNR_{BAC}
FP	$0.16f_{Ny}$	0.33	2.13	6.45	0.52
CCD	$0.10f_{Ny}$	0.10	1.43	14.30	-

and the other to the subsequent contact image calculation (γ). These are also determined with visual inspection of the images and elimination of the edge-enhancement [56]. Fig. 8(a) presents edge-enhanced image and Fig. 8(b) a BAC ($\alpha = 0.07$, and $\gamma = 4$). The BAC is performed using an in-house developed package [57]. As shown by Fig. 8(b) BAC benefits from slightly better CNR than that of edge-enhanced image (Fig. 8(a)), and successfully eliminates the edge-enhancement (Fig. 8(c)). But it's evident from CNR values in Table 1 and image appearance in Fig. 7(b), a Paganin retrieval should be the preferred method in case of FFPE tissue blocks.

V. HIGH-RESOLUTION APPROACHES

One disadvantage of X-ray micro-CT compared to conventional histology is the lower spatial resolution and the non-existing cell specific contrast. To the author's knowledge cellular resolution (depending on the cell types it can vary from few microns down to sub-micron range) has not been reported to date for X-ray micro-CT on standard FFPE blocks using laboratory-based setups. This is a consequence of sheer size of specimen and the amount of material that needs to be penetrated. The former limits the accessible geometrical magnification in cone-beam scanning geometry, while the latter affects the contrast. These together with the limited native X-ray contrast for many cell types, prohibit sufficient cellular resolution and contrast. For a projection image the SNR = $\Delta v \sqrt{N\tau}$, where Δv is the pixel size,

N is the number of photons, and τ is the acquisition time. This fundamental trade-off between resolution, acquisition time, and SNR implies that with the current micro-focus tubes brilliance, sufficient SNR at cellular resolution cannot be achieved. This is as of FFPE blocks dimensions limit our SOD to 15-30mm, resulting in large SDD for sufficient magnification, which comes with SDD^{-2} reduction in photon flux. Furthermore, for the cellular resolution, the tube spot size must be small ($\leq 2\mu m$) that further decreases the photon flux. As a result, for sufficient SNR at cellular resolution, acquisition time becomes impractically long. Nonetheless cellular resolution is not always necessary to find many clinically relevant features for e.g. tumor grading and patient stratification in follicular thyroid carcinomas as shown in our earlier publication [4].

At the whole block scale, resolution will be limited by the sample size to around $15\mu m$ for a 2k $\times$ 2k pixels detector. Fig. 9(a) is a whole block scan, a ROI indicated by white rectangle is digitally magnified and presented in Fig. 9(c). One can utilize classical laminography (CL) to achieve better transverse resolution on the whole block scale, enabling better recognition and identification of finer structures and features of potential clinical utility within practical scanning times. In CL the source and the detector are moved laterally in opposite directions while the FFPE block is fixed (no rotation is done) [58]. This enables small SOD and higher transverse resolution at the expense of anisotropic and lower resolution in the beam direction. Also due to relative motion of the source and detector a single plane of focus along the optical axis is produced, while the out of focus planes contribute to the background intensity, deteriorating the image quality as is illustrated in Fig. 9(b). In order to improve the CL image quality one can use computed laminography (not to be confused with *classical laminography* presented here) where all the planes along the beam direction are in focus [59]. CL is suitable and applied to pseudo-2D specimen, like printed circuit boards. FFPE blocks are not far from pseudo-2D samples considering their $30 \times 25 \times 5mm^3$ dimensions. A CL of the same FFPE block in Fig. 9(a) is presented in Fig. 9(b). The cassette has a significant deteriorating effect on the image quality, contributes significantly to the background. Therefore, if one removes the cassette prior to CL, considerable quality improvement can be expected, though the artifacts and blurring would not be completely eliminated. At the whole block image in Fig. 9(b) the overall quality seems to be worse than that of Fig. 9(a), but a closer look by the digitally magnified image in Fig. 9(d) makes the gain in transversal spatial resolution clear. One can infer from Fig. 9(d) the feature inside the dashed area as a blood vessel while it is not possible to infer the same from Fig. 9(c). The higher transverse resolution can be beneficial in some specific applications were the anisotropic resolution is not a problem.

It is possible to geometrically/optically zoom in on a smaller ROI on the whole block to acquire finer details by performing a local CT (also known as hierachial imaging). This has the benefits of isotropic, small voxel size and no
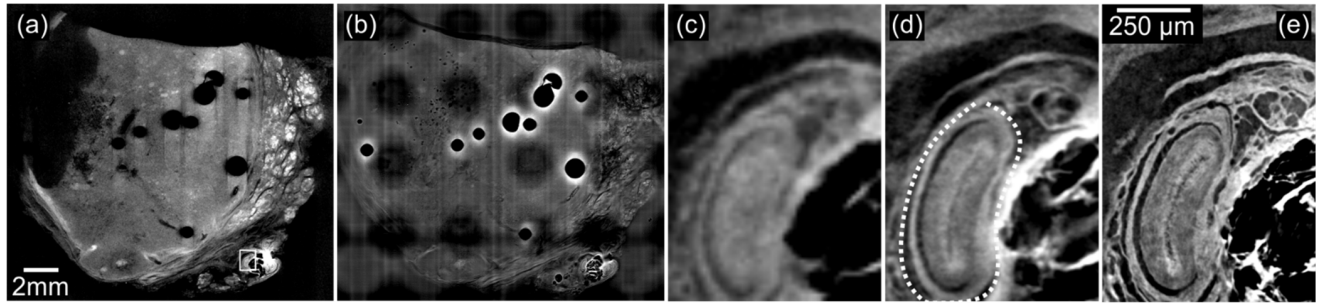
FIGURE 9. Comparison of whole block CT, CL, and Local CT. (a) whole block scan with 15μm voxel size and 01:00 (hh:mm) scanning time. (b) CL of a whole block covering a FoV ca. 20.5 × 20.9mm^2, with 5μm transverse voxel size in 04:36 (hh:mm) theoretical scanning time. (c), and (d) are cropped ROIs from (a), and (b), respectively. ROI is specified by white rectangle in (a). (e) A local scan of the ROI with 2μm voxel size.

major artifacts present. This can be employed by a two-step approach, i. e. first acquiring a whole block CT shown in Fig. 9(a), and in the second step, geometrically zooming in on the ROI and performing a local CT as shown in Fig. 9(e). Detailed scan parameters of Fig. 9 are given in Table S5. It is clear from the image how feature visibility and image quality is enhanced in the ROI by local CT. This is a combined effect of higher spatial resolution as well as the boost in CNR by the pronounced edge-enhancement and subsequent Paganin phase-retrieval (see Table 1).

VI. FUTURE PERSPECTIVES AND OUTLOOK

3D X-ray virtual histology poses great prospect for clinical integration, due to commercial deployment of the recent technological advances in micro-focus X-ray sources and X-ray detectors. To this end we have tested two of the latest generation of commercially available micro-CT scanners with great potential for 3D virtual histology. One is a Phoenix V|tome|x M scanner (Waygate Technologies GmbH & Baker-Hughes, Wunstorf, Germany), and the other one is Polaris (Exciscope AB, Stockholm, Sweden).

Larger detector pixel matrix can be an added advantage when imaging full blocks. A Phoenix V|tome|x M features a Dyn 41|100 detector–a 4k × 4k FP with 100μm physical pixel size. This enables imaging whole blocks with ca. 5μm voxel size. Therefore it benefits from higher resolution and well pronounced edge-enhancement at the whole block level which is not possible with the detectors used in this study.

A workaround for small detectors could be a shift & stitch method by moving laterally (and vertically) a detector for each projection and stitching together several images to form a single projection. Therefore, enabling virtually larger detector pixel matrix. Nevertheless, the increased scan times due to multiple acquisitions per projection and detector movements is a major downside of this option.

We compared EasyTom Ultra XL and the Phoenix experimentally. EasyTom's smaller FP detector matrix achieves a lower resolution at 8.5μm voxel size and smaller FoV ca. 16.1 × 12.8mm^2 Compared to Phoenix's 5μm voxel size, and 20 × 20mm^2 FoV. Fig. 10(a) shows a cropped image of the whole block scan using Phoenix, and Fig. 10(c)
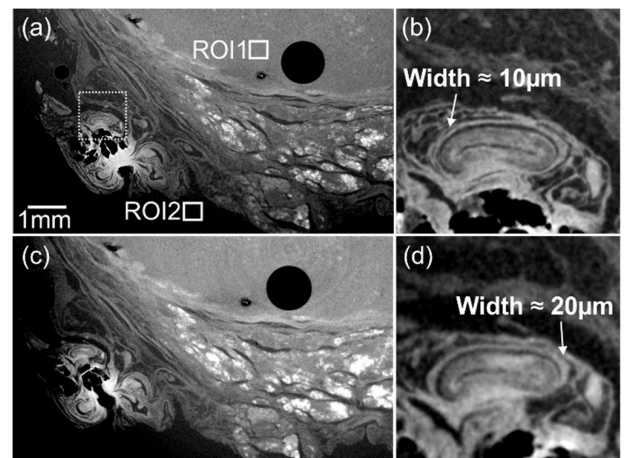
FIGURE 10. Comparison of the (a) Phoenix V|tome|x M with a 4k × 4k 100μm FP and scalable transmission tungsten target tube, and (c) EasyTom with 1880 × 1494 pixel matrix and 127μm pixel size FP, and reflection tungsten target tube. (b) and (d) are corresponding close ups on a feature in the white dashed rectangle in (a) demonstrating the higher resolution and feature visibility by Phoenix.

shows a cropped image of EasyTom scan. The exact scan parameters can be found in Table S6. CNR between tissue (ROI1), and wax (ROI2) are 10.92, and 10.22 for the Phoenix and EasyTom, respectively. Fig. 10(b), and (d) are close ups of a ROI given by the dashed line in Fig. 10(a) to demonstrate smallest possible detectable feature and the general feature visibility. For Phoenix scan, the smallest feature is approximately 10μm in width shown in Fig. 10(b), and for that of EasyTom is about 20μm, presented in Fig. 10(d). In conclusion, Phoenix V|tome|x M provides two times better resolution with a comparable CNR within comparable scan times. Based on the disclosed system and scan parameters, we expect the photon intensity to be lower in the Phoenix scan compared to EasyTom scan. Therefore, this comparable CNR can be attributed to the higher edge-enhancement and contrast contribution from XPCI. Simulations of the edge-enhancement visibility for the Dyn 41|100 detector is shown in Fig. 11(a). This illustrates the improved edge-enhancement visibility compared to EasyTom XL Ultra (see Fig 6(a)) due to smaller detector pixel size.

It also demonstrates the possibility of PBI at $5\mu m$ voxel size and sufficiently long SDD (SDD>900mm). The simulation parameters for Fig. 11(a) are 2 pixels at FWHM detector PSF as supplied by the vendor, and $9\mu m$ tube spots size in accordance with the scan parameters in Fig. 11(b).
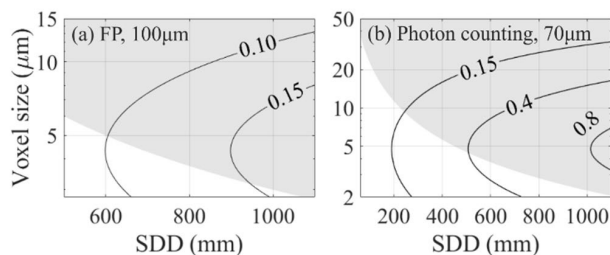

FIGURE 11. Visibility of edge-enhancement for (a) Phoenix V|tome|x M 100μm FP with 2 pixel PSF, here source spot size is considered to be 9μm in order to simulate the scan presented in Fig. 9(a). (b) DECTRIS EIGER2 series with 70μm pixels size, 1 pixel PSF, and 5μm tube spot size.

Another interesting development is the expected future broad introduction of photon counting detectors into commercial micro-CT scanners [60], [61]. They have a single-pixel PSF which is a great advantage for PBI. They also eliminate readout noise, and dark current. We applied the edge-enhancement visibility simulation as an illustrative example for a DECTRIS EIGER2 series with $75\mu m$ pixel size, one pixel PSF [62], and the tube spot size was considered to be $5\mu m$. The result is presented in Fig 11(b). The figure illustrates the very high edge-enhancement visibility that would be achievable with such a setup. Adding to this the high efficiency of cadmium telluride converter in these detectors, as well as superior noise characteristics, photon counting detectors could offer an exciting opportunity for superior PBI for 3D virtual histopathology of FFPE blocks.

Developments in micro-focus X-ray tubes also show very positive prospect with the advent of liquid-metal-jet anode sources [63]. Liquid-metal-jet sources can provide much higher (up to about 10 times) photon flux compared to conventional micro-focus tubes. Moreover, their emission spectra is more suitable for PBI and soft tissues as the mean energy is lower compared to tungsten target tubes. On the other hand, the tube spot size is not as small as high-end tungsten target micro/nano-focus tubes. It is asymmetric and at its smallest extension is $10\mu m$. This may limit their applicability to for high-resolution PBI however, they offer very interesting perspectives for whole block PBI, where tube spot size resolution of $10\mu m$ is sufficient and one can enjoy a more suitable spectrum with high photon flux. To be applicable to higher resolution PBI, a high-resolution detector and an inverse (small-magnification) geometry has to be employed. This is possible thanks to the high photon flux, but the FoV is much more limited.

Fig. 12 compares scans from (a) Polaris, a phase-contrast micro-CT scanner from Exciscope, with a liquid-metal jet source, and (c) EasyTom with scan time 03:00, and 3:16 (hh:mm), respectively. Details of scans settings are provided
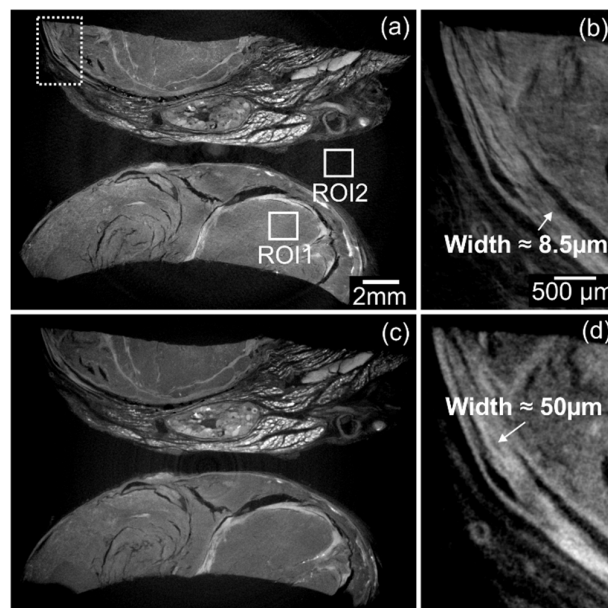
FIGURE 12. A comparison between (a) Polaris scanner with liquid-metal-jet-anode source, and a 13.1μm sCMOS, and (c) EasyTom XL Ultra with a solid reflection tungsten anode, and 127μm FP. Exact scan parameters are provided in the Table S6.

in the Table S6. Here in Fig. 12(a), and (b) we benefit from ca. 145mm Z_{eff}, and in Fig. 12(c), and (d) ca. 40mm Z_{eff}. This large Z_{eff} is made possible because of small native pixel size ($13.1\mu m$) of the Polaris sCMOS alongside with its 4k matrix, making it suitable for whole block PBI. The voxel size of the Polaris scan is 3.5, and $14\mu m$ for EasyTom. Close ups of the white dashed line ROI in Fig 12(a) are presented in Fig. 12(b), and (d). The smallest features visible are pointed out by arrows in Fig. 12(b) for Polaris (width $\simeq$ $8.5\mu m$), and Fig. 12(d) for EasyTom (width $\simeq 50\mu m$). The CNR between ROI1 (tissue), and ROI2 (wax) were 8.60 for Polaris, and 7.60 for EasyTom. Note that here we use the CNRs just for indicative comparison. They are influenced by many system and scan parameters such as geometry, X-ray spectrum, and the corresponding choice of Paganin retrieval, just to mention a few, which are distinctly different for the two cases. In conclusion, Polaris with its high-output liquid-metal-jet anode source provides four times better resolution, with slightly better CNR, at a comparable scanning time compared to EasyTom XL Ultra. Previously, Polaris has been benchmarked against synchrotron radiation-based imaging and other state-of-the-art scanner which can be interesting to look into as well [16].

VII. CONCLUSION
In conclusion, micro-CT emerges as a flexible and versatile tool, demonstrating considerable promise for X-ray 3D virtual histology. We have outlined methods to mitigate artifacts and explored two potential positioning approaches for FFPE blocks, focusing on CNR and imaging artifacts. Our investigation revealed a global optimal tube voltage for tungsten target tubes, highlighting a critical parame-

ter for achieving optimal results. Additionally, we have demonstrated the feasibility of PC imaging on FFPE blocks, particularly also at whole block scale with a suitable large-matrix detector. While Paganin phase-retrieval emerges as a valuable technique for enhancing image quality, BAC has proven suboptimal/inadequate, specifically for FFPE blocks. Classical laminography, including more advanced computed laminography, offers a pathway to achieve higher transverse spatial resolution, albeit with sacrificing the axial resolution and added artifacts. Conversely, local CT presents an avenue for achieving very high resolutions with comparatively minimal artifacts and benefiting from enhanced phase effects. Optimizations presented here are generic and can be relevant to any other laboratory-based scanner with a tungsten target source in cone-beam geometry. The future of X-ray 3D virtual histology is definitely promising, with anticipated improvements in image quality driven by the advent of powerful liquid-metal-jet anode sources, advancements in detector technology, including larger matrices yet smaller pixel sizes, and the utilization of photon-counting detectors.

DISCLOSURE

REFERENCES

[1] A. L. Kiemen, A. I. Damanakis, A. M. Braxton, J. He, D. Laheru, E. K. Fishman, P. Chames, C. A. Pérez, P.-H. Wu, D. Wirtz, L. D. Wood, and R. H. Hruban, "Tissue clearing and 3D reconstruction of digitized, serially sectioned slides provide novel insights into pancreatic cancer," *Med*, vol. 4, no. 2, pp. 75–91, Feb. 2023.

[2] G. O. B. Braga, R. Zboray, A. Parrilli, M. Bulatovic, M. D. Caversaccio, and F. Wagner, "Otosclerosis under microCT: New insights into the disease and its anatomy," *Frontiers Radiol.*, vol. 2, Aug. 2022, Art. no. 965474.

[3] L. Massimi, I. Bukreeva, G. Santamaria, M. Fratini, A. Corbelli, F. Brun, S. Fumagalli, L. Maugeri, A. Pacureanu, P. Cloetens, N. Pieroni, F. Fiordaliso, G. Forloni, A. Uccelli, N. K. de Rosbo, C. Balducci, and A. Cedola, "Exploring Alzheimer's disease mouse brain through X-ray phase contrast tomography: From the cell to the organ," *NeuroImage*, vol. 184, pp. 490–495, Jan. 2019.

[4] K. Tajbakhsh, O. Stanowska, A. Neels, A. Perren, and R. Zboray, "3D virtual histopathology by phase-contrast X-ray micro-CT for follicular thyroid neoplasms," *IEEE Trans. Med. Imag*, Mar. 2024, doi: 10.1109/TMI.2024.3372602.

[5] J. Pichat, J. E. Iglesias, T. Yousry, S. Ourselin, and M. Modat, "A survey of methods for 3D histology reconstruction," *Med. Image Anal.*, vol. 46, pp. 73–105, May 2018.

[6] T. S. Haddad, P. Friedl, N. Farahani, D. Treanor, I. Zlobec, and I. Nagtegaal, "Tutorial: Methods for three-dimensional visualization of archival tissue material," *Nature Protocols*, vol. 16, no. 11, pp. 4945–4962, Oct. 2021.

[7] J. Albers, S. Pacilé, M. A. Markus, M. Wiart, G. Vande Velde, G. Tromba, and C. Dullin, "X-ray-Based 3D virtual histology—Adding the next dimension to histological analysis," *Mol. Imag. Biol.*, vol. 20, no. 5, pp. 732–741, Oct. 2018.

[8] J. D. Boerckel, D. E. Mason, A. M. McDermott, and E. Alsberg, "Micro-computed tomography: Approaches and applications in bioengineering," *Stem Cell Res. Therapy*, vol. 5, no. 6, p. 144, Dec. 2014.

[9] O. L. Katsamenis, M. Olding, J. A. Warner, D. S. Chatelet, M. G. Jones, G. Sgalla, B. Smit, O. J. Larkin, I. Haig, L. Richeldi, I. Sinclair, P. M. Lackie, and P. Schneider, "X-ray micro-computed tomography for nondestructive three-dimensional (3D) X-ray histology," *Amer. J. Pathol.*, vol. 189, no. 8, pp. 1608–1620, Aug. 2019.

[10] V. Cnudde, B. Masschaele, H. E. V. De Cock, K. Olstad, L. Vlaminck, J. Vlassenbroeck, M. Dierick, Y. D. Witte, L. Van Hoorebeke, and P. Jacobs, "Virtual histology by means of high-resolution X-ray CT," *J. Microsc.*, vol. 232, no. 3, pp. 476–485, Dec. 2008.

[11] L. A. Walton, R. S. Bradley, P. J. Withers, V. L. Newton, R. E. B. Watson, C. Austin, and M. J. Sherratt, "Morphological characterisation of unstained and intact tissue micro-architecture by X-ray computed micro- and nano-tomography," *Sci. Rep.*, vol. 5, no. 1, pp. 1–14, May 2015.

[12] C. Raven, A. Snigirev, I. Snigireva, P. Spanne, A. Souvorov, and V. Kohn, "Phase-contrast microtomography with coherent high-energy synchrotron X rays," *Appl. Phys. Lett.*, vol. 69, no. 13, pp. 1826–1828, Sep. 1996.

[13] G. Rodgers, C. Bikis, P. Janz, C. Tanner, G. Schulz, P. Thalmann, C. A. Haas, and B. Müller, "3D X-ray histology for the investigation of temporal lobe epilepsy in a mouse model," *Microsc. Microanal.*, vol. 29, no. 5, pp. 1730–1745, Sep. 2023.

[14] A. Khimchenko, C. Bikis, A. Pacureanu, S. E. Hieber, P. Thalmann, H. Deyhle, G. Schweighauser, J. Hench, S. Frank, M. Muller-Gerbl, and G. Schulz, "Hard X-ray nanoholotomography: Large-scale, label-free, 3D neuroimaging beyond optical limit," *Adv. Sci.*, vol. 5, no. 6, Jun. 2018, Art. no. 1700694.

[15] A. Pogany, D. Gao, and S. W. Wilkins, "Contrast and resolution in imaging with a microfocus X-ray source," *Rev. Sci. Instrum.*, vol. 68, no. 7, pp. 2774–2782, Jul. 1997.

[16] A. Migga, G. Schulz, G. Rodgers, M. Osterwalder, C. Tanner, H. Blank, I. Jerjen, P. Salmon, W. Twengström, M. Scheel, T. Weitkamp, C. M. Schlepütz, J. S. Bolten, J. Huwyler, G. Hotz, S. Madduri, and B. Müller, "Comparative hard X-ray tomography for virtual histology of zebrafish larva, human tooth cementum, and porcine nerve," *J. Med. Imag.*, vol. 9, no. 3, Mar. 2022, Art. no. 031507.

[17] P. Bidola, K. Morgan, M. Willner, A. Fehringer, S. Allner, F. Prade, F. Pfeiffer, and K. Achterhold, "Application of sensitive, high-resolution imaging at a commercial lab-based X-ray micro-CT system using propagation-based phase retrieval," *J. Microsc.*, vol. 266, no. 2, pp. 211–220, May 2017.

[18] B. Zeller-Plumhoff, J. L. Mead, D. Tan, T. Roose, G. F. Clough, R. P. Boardman, and P. Schneider, "Soft tissue 3D imaging in the lab through optimised propagation-based phase contrast computed tomography," *Opt. Exp.*, vol. 25, no. 26, pp. 33451–33468, Dec. 2017.

[19] L. Brombal, G. Kallon, J. Jiang, S. Savvidis, P. De Coppi, L. Urbani, E. J. Forty, R. C. Chambers, R. Longo, A. Olivo, and M. Endrizzi, "Monochromatic propagation-based phase-contrast microscale computed-tomography system with a rotating-anode source," *Phys. Rev. Appl.*, vol. 11, no. 3, Mar. 2019, Art. no. 034004.

[20] S. C. Mayo, A. W. Stevenson, and S. W. Wilkins, "In-line phase-contrast X-ray imaging and tomography for materials science," *Materials*, vol. 5, no. 12, pp. 937–965, May 2012.

[21] B. Xu, A. Teplov, K. Ibrahim, T. Inoue, B. Stueben, N. Katabi, M. Hameed, Y. Yagi, and R. Ghossein, "Detection and assessment of capsular invasion, vascular invasion and lymph node metastasis, volume in thyroid carcinoma using microCT scanning of paraffin tissue blocks (3D whole block imaging): A proof of concept," *Mod. Pathol.*, vol. 33, no. 12, pp. 2449–2457, Dec. 2020.

[22] W. Twengström, C. F. Moro, J. Romell, J. C. Larsson, E. Sparrelid, M. Björnstedt, and H. M. Hertz, "Can laboratory X-ray virtual histology provide intraoperative 3D tumor resection margin assessment?" *J. Med. Imag.*, vol. 9, no. 3, Feb. 2022, Art. no. 031503.

[23] M. Töpperwien, A. Markus, F. Alves, and T. Salditt, "Contrast enhancement for visualizing neuronal cytoarchitecture by propagation-based X-ray phase-contrast tomography," *NeuroImage*, vol. 199, pp. 70–80, Oct. 2019.

[24] M. G. Jones, A. Fabre, P. Schneider, F. Cinetto, G. Sgalla, M. Mavrogordato, S. Jogai, A. Alzetani, B. G. Marshall, K. M. A. O'Reilly, J. A. Warner, P. M. Lackie, D. E. Davies, D. M. Hansell, A. G. Nicholson, I. Sinclair, K. K. Brown, and L. Richeldi, "Three-dimensional characterization of fibroblast foci in idiopathic pulmonary fibrosis," *JCI Insight*, vol. 1, no. 5, pp. 1–11, Apr. 2016.

[25] A. E. Scott, D. M. Vasilescu, K. A. D. Seal, S. D. Keyes, M. N. Mavrogordato, J. C. Hogg, I. Sinclair, J. A. Warner, T.-L. Hackett, and P. M. Lackie, "Three dimensional imaging of paraffin embedded human lung tissue samples by micro-computed tomography," *PLoS ONE*, vol. 10, no. 6, Jun. 2015, Art. no. e0126230.

[26] S. E. Schrup, T. de Bel, T. Hoskin, T. Allers, S. Winham, D. Radisky, L. Pacheco-Spann, L. Seymour, A. Degnim, and M. Sherman, "Abstract 3587: High resolution microCT to analyze the 3D morphology of microcalcifications in benign breast disease and breast cancer biopsy tissues," *Cancer Res.*, vol. 83, p. 3587, Apr. 2023.

[27] L. M. Arana Peña, S. Donato, D. Bonazza, L. Brombal, F. Martellani, F. Arfelli, G. Tromba, and R. Longo, "Multiscale X-ray phase-contrast tomography: From breast CT to micro-CT for virtual histology," *Phys. Medica*, vol. 112, Aug. 2023, Art. no. 102640.

[28] M. Reichardt, M. Töpperwien, A. Khan, F. Alves, and T. Salditt, "Fiber orientation in a whole mouse heart reconstructed by laboratory phase-contrast micro-CT," *J. Med. Imag.*, vol. 7, no. 2, Mar. 2020, Art. no. 023501.

[29] J. N. Clark, A. Garbout, S. A. Ferreira, B. Javaheri, A. A. Pitsillides, S. M. Rankin, J. R. T. Jeffers, and U. Hansen, "Propagation phase-contrast micro-computed tomography allows laboratory-based three-dimensional imaging of articular cartilage down to the cellular level," *Osteoarthritis Cartilage*, vol. 28, no. 1, pp. 102–111, Jan. 2020.

[30] S. Saghamanesh, D. Dumitriu Lagrange, P. Reymond, I. Wanke, K.-O. Lövblad, A. Neels, and R. Zboray, "Non contrast enhanced volumetric histology of blood clots through high resolution propagation-based X-ray microtomography," *Sci. Rep.*, vol. 12, no. 1, p. 2778, Feb. 2022.

[31] M. Töpperwien, F. van der Meer, C. Stadelmann, and T. Salditt, "Correlative X-ray phase-contrast tomography and histology of human brain tissue affected by Alzheimer's disease," *NeuroImage*, vol. 210, Apr. 2020, Art. no. 116523.

[32] C. Han and J. Baek, "Multi-pass approach to reduce cone-beam artifacts in a circular orbit cone-beam CT system," *Opt. Exp.*, vol. 27, no. 7, pp. 10108–10126, Mar. 2019.

[33] S. Choi, J. Kim, and J. Baek, "A hybrid approach to reduce cone-beam artifacts for a circular orbit cone-beam CT system," *IEEE Access*, vol. 6, pp. 54595–54606, 2018.

[34] S. Handschuh, C. T. C. Okada, I. Walter, C. Aurich, and M. Glösmann, "An optimized workflow for microCT imaging of formalin-fixed and paraffin-embedded (FFPE) early equine embryos," *Anatomia, Histologia, Embryologia*, vol. 51, no. 5, pp. 611–623, Jul. 2022.

[35] A. D. Plessis, C. Broeckhoven, A. Guelpa, and S. G. L. Roux, "Laboratory X-ray micro-computed tomography: A user guideline for biological samples," *GigaScience*, vol. 6, no. 6, pp. 1–11, Jun. 2017.

[36] A. Teplov, K. Tabata, X. Fu, N. Uraoka, M. H. A. Roehrl, P. Ntiamoah, J. L. Humm, S. J. Sirintrapun, M. P. Murray, J. Shia, and W. D. Travis, "Development of standard operating procedure (SOP) of micro-computed tomography (micro-CT) in pathology," *Diagn. Pathol.*, vol. 5, no. 1, Jul. 2019.

[37] A. Deresch, "Modellierung von röntgenspektren für technische anwendungen," Ph.D. theses, Dept. Mathematisch-Naturwissenschaftliche Fakultät / Institut für Physik und Astronomie, Universitäät Potsdam, Germany, Tech. Rep., 2015.

[38] M. J. Berger, *XCOM: Photon Cross Sections Database*, Standard 87–3597, NIST Standard Reference Database, Jan. 2009.

[39] L. A. Feldkamp, L. C. Davis, and J. W. Kress, "Practical cone-beam algorithm," *J. Opt. Soc. Amer. A, Opt. Image Sci.*, vol. 1, no. 6, pp. 612–619, Jun. 1984.

[40] F. Pfeiffer, C. Kottler, O. Bunk, and C. David, "Hard X-ray phase tomography with low-brilliance sources," *Phys. Rev. Lett.*, vol. 98, no. 10, Mar. 2007, Art. no. 108105.

[41] K. Tajbakhsh, S. Ebrahimi, and M. Dashtdar, "Low-coherence quantitative differential phase-contrast microscopy using Talbot interferometry," *Appl. Opt.*, vol. 61, no. 2, pp. 398–402, Jan. 2022.

[42] A. Olivo, "Edge-illumination X-ray phase-contrast imaging," *J. Phys., Condens. Matter*, vol. 33, no. 36, Jul. 2021, Art. no. 363002.

[43] I. Zanette, T. Zhou, A. Burvall, U. Lundström, D. H. Larsson, M. Zdora, P. Thibault, F. Pfeiffer, and H. M. Hertz, "Speckle-based X-ray phase-contrast and dark-field imaging with a laboratory source," *Phys. Rev. Lett.*, vol. 112, no. 25, Jun. 2014, Art. no. 253903.

[44] S. W. Wilkins, T. E. Gureyev, D. Gao, A. Pogany, and A. W. Stevenson, "Phase-contrast imaging using polychromatic hard X-rays," *Nature*, vol. 384, no. 6607, pp. 335–338, Nov. 1996.

[45] C. Zuo, J. Li, J. Sun, Y. Fan, J. Zhang, L. Lu, R. Zhang, B. Wang, L. Huang, and Q. Chen, "Transport of intensity equation: A tutorial," *Opt. Lasers Eng.*, vol. 135, Dec. 2020, Art. no. 106187.

[46] T. E. Gureyev, Y. I. Nesterets, A. W. Stevenson, P. R. Miller, A. Pogany, and S. W. Wilkins, "Some simple rules for contrast, signal-to-noise and resolution in in-line X-ray phase-contrast imaging," *Opt Exp.*, vol. 16, no. 5, pp. 3223–3241, Feb. 2008.

[47] A. Balles, S. Zabler, T. Ebensperger, C. Fella, and R. Hanke, "Propagator based formalism for optimizing in-line phase contrast imaging in laboratory X-ray setups," *Rev. Sci. Instrum.*, vol. 87, no. 9, pp. 093707-1–093707-9, Sep. 2016.

[48] K. Tajbakhsh. *TIE4PBI*. Accessed: May 1, 2024. [Online]. Available: https://github.com/kiataj/TIE4PBI

[49] D. M. Paganin and D. Pelliccia, "Tutorials on X-ray phase contrast imaging: Some fundamentals and some conjectures on future developments," 2019, *arXiv:1902.00364*.

[50] D. Paganin, S. C. Mayo, T. E. Gureyev, P. R. Miller, and S. W. Wilkins, "Simultaneous phase and amplitude extraction from a single defocused image of a homogeneous object," *J. Microsc.*, vol. 206, no. 1, pp. 33–40, Apr. 2002.

[51] W. Vagberg, J. Persson, L. Szekely, and H. M. Hertz, "Cellular-resolution 3D virtual histology of human coronary arteries using X-ray phase tomography," *Sci. Rep.*, vol. 8, no. 1, p. 11014, Jul. 2018.

[52] J. Romell, W. Vagberg, M. Romell, S. Häggman, S. Ikram, and H. M. Hertz, "Soft-tissue imaging in a human mummy: Propagation-based phase-contrast CT," *Radiology*, vol. 289, no. 3, pp. 670–676, Dec. 2018.

[53] M. Krenkel, M. Töpperwien, C. Dullin, F. Alves, and T. Salditt, "Propagation-based phase-contrast tomography for high-resolution lung imaging with laboratory sources," *AIP Adv.*, vol. 6, no. 3, Mar. 2016, Art. no. 035007.

[54] A. V. Bronnikov, "Reconstruction formulas in phase-contrast tomography," *Opt. Commun.*, vol. 171, nos. 4–6, pp. 239–244, Dec. 1999.

[55] Y. De Witte, M. Boone, J. Vlassenbroeck, M. Dierick, and L. Van Hoorebeke, "Bronnikov-aided correction for X-ray computed tomography," *J. Opt. Soc. Amer. A, Opt. Image Sci.*, vol. 26, no. 4, pp. 890–894, Mar. 2009.

[56] T. Salditt, T. Aspelmeier, and S. Aeffner, *Biomedical Imaging: Principles of Radiography, Tomography and Medical Physics*. Berlin, Germany: Walter de Gruyter GmbH & Co KG, 2017, ch. 6.

[57] J. Hofmann and R. Zboray, "An in-house cone-beam tomographic reconstruction package for laboratory X-ray phase-contrast imaging," *Appl. Sci.*, vol. 12, no. 3, p. 1430, Dec. 2022.

[58] D. T. Nguyen, T. C. Larsen, M. Wang, R. H. Knutsen, Z. Yang, E. E. Bennett, D. Mazilu, Z. Yu, X. Tao, D. R. Donahue, A. M. Gharib, C. K. E. Bleck, J. Moss, A. T. Remaley, B. A. Kozel, and H. Wen, "X-ray microtomosynthesis of unstained pathology tissue samples," *J. Microsc.*, vol. 283, no. 1, pp. 9–20, Feb. 2021.

[59] J. Zhou, M. Maisl, H. Reiter, and W. Arnold, "Computed laminography for materials testing," *Appl. Phys. Lett.*, vol. 68, no. 24, pp. 3500–3502, Jun. 1996.

[60] T. Flohr and B. Schmidt, "Technical basics and clinical benefits of photon-counting CT," *Investigative Radiol.*, vol. 58, no. 7, pp. 441–450, Jul. 2023.

[61] M. Danielsson, M. Persson, and M. Sjölin, "Photon-counting X-ray detectors for CT," *Phys. Med. Biol.*, vol. 66, no. 3, Jan. 2021, Art. no. 03TR01.

[62] A. Förster, S. Brandstetter, M. Müller, and C. Schulze-Briese, "EIGER detectors in biological crystallography," DECTRIS Ltd., Baden-Dättwil, Switzerland, White Paper, May 2016.

[63] H. Hertz, "Liquid-metal-jet X-ray sources and high-resolution biomedical imaging," in *Proc. APS March Meeting Abstr.*, Jan. 2018, pp. 1–5. [Online]. Available: https://ui.adsabs.harvard.edu/abs/2018APS.MARL05002H

KIARASH TAJBAKHSH received the bachelor's degree in physics and the master's degree in optics and laser physics from Shahid Beheshti University, Tehran, Iran. He is currently pursuing the Ph.D. degree in materials science with the Empa–Swiss Federal Laboratories for Materials Science and Technology, Switzerland, and the University of Fribourg, Switzerland. His research interests include X-ray phase-contrast imaging, radiogenomics, and computer science.

ANTONIA NEELS received the Ph.D. degree in science from the University of Neuchâtel, Switzerland. She studied chemistry from the Humboldt University of Berlin, Germany. She has been leading the XRD Laboratory, CSEM/EPFL, and heads the Center for X-ray Analytics, Empa. She is currently a Titular Professor with the University of Fribourg, Switzerland. She also studies novel materials with fascinating structures leading to new physical properties and applications. She has published more than 300 papers and is active in national and international crystallographic associations and commissions. Her interest in developing X-ray-based analytical concepts is directed toward strain and defect mobility in order/disorder materials, especially for space and biomedical applications.

ELENA FADEEVA received the B.Sc. and M.Sc. degrees in biomedical engineering from the Technical University of Kaiserlautern-Landau. She is currently pursuing the Ph.D. degree in physics with Leibniz University Hannover. She is also the Sales Manager for industrial radiography systems at Waygate Technologies. She worked on super-hydrophobic surfaces on metals for biomedical applications.

JAKOB C. LARSSON received the master's degree in engineering physics from the KTH Royal Institute of Technology, in 2013, and the Ph.D. degree from the Laboratory X-Ray Fluorescence Tomography. He was a Postdoctoral Researcher in X-ray phase-contrast imaging. In 2019, he co-founded the company Exciscope AB, bringing the research about X-ray phase contrast into a commercial product.

OLGA STANOWSKA received the degree from the Medical University of Warsaw, Poland, in 2011. After completing pathology residency in Warsaw and Bern, she is currently practicing as a Consultant Pathologist specializing in head and neck pathology and researching on thyroid cancer with the Institute for Tissue Medicine and Pathology, University of Bern.

AUREL PERREN trained in pathology in Zürich and moved to the Technical University of Munich as a Professor of tumor pathology for three years. In 2009, he was the Head of the Institute of Tissue Medicine and Pathology, University of Bern. He specializes in endocrine tumor pathology and the development of endocrine tumors. Since 2003, he has been involved in the WHO classification refinements. He represents the view of tissue medicine/pathology and the molecular basis of tumorigenesis in various guidelines, in particular in the European Neuroendocrine Tumor Society ENETS guidelines.

ROBERT ZBORAY received the M.Sc. degree in applied physics from the Technical University of Budapest, Hungary, and the Ph.D. degree in nuclear engineering from Delft University of Technology, The Netherlands. Later, he has been with the Paul Scherrer Institute, Switzerland, as a Senior Research Scientist. He is currently the Group Leader for X-Ray Imaging with the Centre for X-ray Analytics, Empa. Before joining Empa, he held a professorship at Penn State University, USA. His recent research interests include novel, multi-modal X-ray imaging techniques for biomedical applications, and image processing methods.

● ● ●